Valley-Selective Klein Tunneling through a Superlattice Barrier in Graphene

Xing-Tao An[1,*,†] and Wang Yao[2,‡]

[1] *School of Science, Hebei University of Science and Technology, Shijiazhuang, Hebei 050018, China*
[2] *Department of Physics, University of Hong Kong, Hong Kong, China*

(Received 17 February 2020; revised 25 March 2020; accepted 26 June 2020; published 14 July 2020)

Graphene electrons feature a pair of massless Dirac cones of opposite pseudospin chirality at two valleys. Klein tunneling refers to the intriguing capability of these chiral electrons to penetrate through a high and wide potential barrier. The two valleys have been treated independently in the literature, where time-reversal symmetry dictates that neither the normal incidence transmission nor the angle-averaged one can have any valley polarization. Here, we show that, when intervalley scattering by a barrier is accounted for, graphene electrons normally incident at a superlattice barrier can experience fully valley-selective Klein tunneling, i.e., perfect transmission in one valley and perfect reflection in the other. Intervalley backscattering creates staggered pseudospin gaps in the superlattice barrier, which, combined with the valley contrast in pseudospin chirality, determines the valley polarity of Klein tunneling. The angle-averaged transmission can have a net valley polarization of 20% for a five-period barrier and exceed 75% for a 20-period barrier. Our finding points to an unexpected opportunity to realize valley functionalities in graphene electronics.

DOI: 10.1103/PhysRevApplied.14.014039

I. INTRODUCTION

The chiral nature of relativistic electrons results in their counterintuitive scattering behavior at potential barriers, known as the Klein paradox [1]. The chiral Dirac quasiparticles in graphene make a condensed matter test bed possible for this exotic consequence of quantum electrodynamics [2]. Upon normal incidence at a barrier, the Klein paradox manifests either as perfect transmission in single-layer graphene or as perfect reflection in bilayer graphene. This difference between the two graphene systems arises from their distinct chirality structures associated with the *sublattice pseudospin*, which dictate either forward propagation inside the barrier or that backscattering is allowed under pseudospin conservation. The electron mean free path can reach tens of microns in high-quality graphene [3,4], which is promising for the exploitation of the coherent chiral tunneling effect for electron devices with optics analogs [5–12].

Graphene electrons also feature a valley degree of freedom, which results in labeling of the two massless Dirac cones with *opposite* pseudospin chirality at the K and $-K$ corners of the Brillouin zone. The possibility of addressing and exploiting the valley as an information carrier has led to conceptual electronic applications known as valleytronics [13–15]. The valley-selective flow of carriers, or valley current, is the main element that enables valley functionalities. A variety of schemes are explored for producing a valley current in graphene by introducing edges [14], inversion symmetry breaking [15–19], line defects, and topological interfaces [20–25], or by exploiting strains [26,27] and trigonal warping [28]. In the context of Klein tunneling, there is the possibility of engineering valley-polarized transmission at selected oblique angles [9,29], but the angle-averaged transmission cannot carry valley polarization, as a consequence of time-reversal symmetry [30], limiting such schemes to ballistic devices and angle-resolved operations. All of the above mechanisms exploit the intravalley process only, whereas intervalley scattering is generally considered as a deleterious cause of error for the valley functionalities. On the other hand, a counterintuitive role of intervalley scattering in pumping valley polarization has been revealed in recent theoretical studies [30,31].

Here, we discover that, at a superlattice barrier in single-layer graphene, intervalley scattering can selectively block Klein tunneling in a chosen valley, while retaining perfect transmission in the other. This valley selectivity is made possible by the staggered pseudospin gaps created by intervalley backscattering in the superlattice barrier. For an electrostatically defined superlattice, gate control of the barrier height can be used to switch the valley polarity of Klein tunneling. The angle-averaged transmission can have a net valley polarization of 20% for a five-period barrier and exceed 75% for a 20-period barrier, where the total width of the superlattice can be practically restricted in the

*anxingtao@semi.ac.cn
†anxt2005@163.com
‡wangyao@hku.hk

submicron regime using O(10) nanometer periodicity. This chiral tunneling phenomenon makes a high-throughput valley filter possible, where the sizeable angle-integrated valley polarity is crucial for harvesting the filtered valley current beyond the ballistic limit.

II. RESULTS

A. Staggered pseudospin gaps in graphene superlattices

Let us consider single-layer graphene subject to a Kronig-Penney-type electrostatic potential along the zigzag direction, with square barriers of width W and height U arranged with periodicity L [Fig. 1(a)]. The effect of such a superlattice on massless chiral electrons is investigated in the absence of intervalley scattering [7]. Intravalley scattering by the superlattice potential leads to anisotropic massless Dirac dispersion: the group velocity is renormalized in the armchair (y) direction parallel to the barriers, but unchanged in the perpendicular zigzag (x) direction, as a manifestation of the Klein paradox. The step-shaped potential can also introduce intervalley scattering that couples the two valleys, which, however, is not considered in the literature.

To understand the role of intervalley scattering in such graphene superlattices, we first analyze the propagation of an electron wave function in a single period, as Fig. 1(b) illustrates. For normal incidence at the barrier, intravalley backscattering is forbidden by the orthogonality in the pseudospin of the initial and final states. Nevertheless, two intervalley backscattering channels are allowed at the potential steps, for pseudospins in the $+x$ and $-x$ orientations. At the Fermi energy (E_f), the propagation of pseudospin $|-x\rangle$ is through the valence-band states of wavevector $\pm(K - q_h)$ in the barrier region of width W, while, in the well region of width $L - W$, it is through the conduction-band states of wavevector $\pm(K + q_e)$.

These wavevectors, together with the width of the barrier region and well region, determine the condition for maximum constructive interference for transmission through a single period of the superlattice. For pseudospin $|-x\rangle$, the condition reads

$$K - q_h = n\frac{\pi}{W}, \quad K + q_e = m\frac{\pi}{L - W}, \tag{1}$$

where n and m are integers. From the linear dispersion, we have $\hbar v_0(q_e + q_h) = U$. When Eq. (1) is satisfied, perfect transmission (Klein tunneling) is still expected for

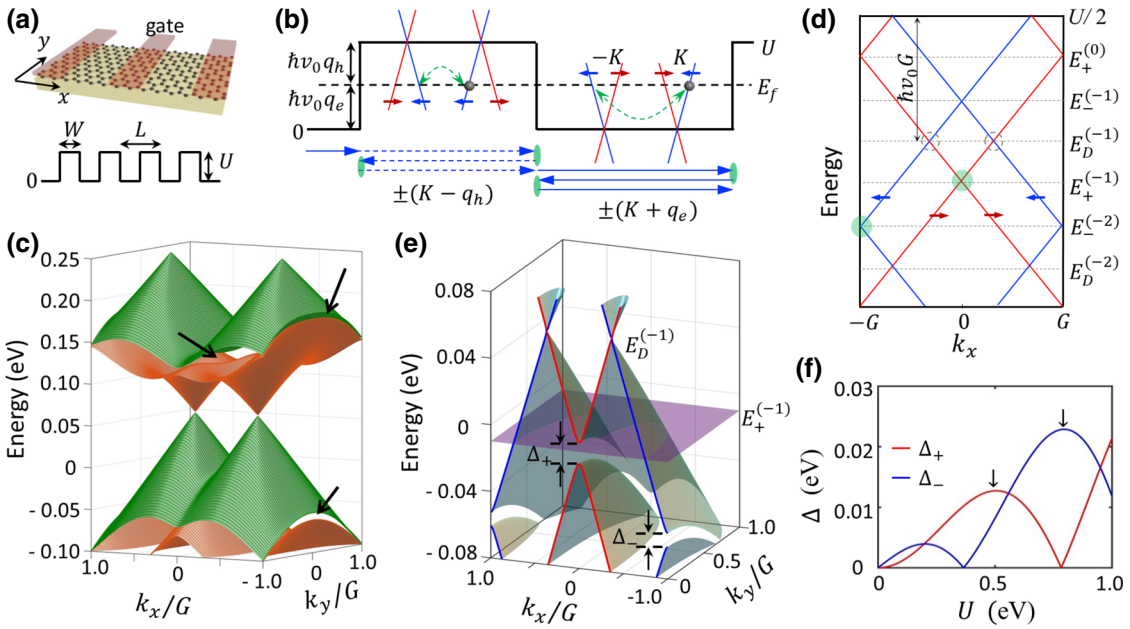

FIG. 1. Staggered pseudospin gaps by intervalley scattering. (a) Schematic of an electrostatically defined superlattice potential. (b) Backscattering at the potential steps can happen only through the pseudospin-conserving intervalley process. Red and blue arrows denote pseudospins $|+x\rangle$ and $|-x\rangle$, respectively. Blue lines with arrows denote propagation in the pseudospin $|-x\rangle$ state, with wavevectors $\pm(K + q_e)$ and $\pm(K - q_h)$, respectively, in the well and barrier regions. (c) Example of superlattice miniband dispersion, with $U = 0.5$ eV, $L = 40a \approx 10$ nm, and $W = 20a \approx 5$ nm; a is the lattice constant of graphene. (d) Schematic zone-folding scheme, plotted at $k_y = 0$, for the superlattice in (c). States of $|+x\rangle$ and $|-x\rangle$ pseudospin are color coded in red and blue, respectively. With energy set to zero at the potential bottom, the original Dirac points are at $U/2$. Intersections between bands of common pseudospin can be gapped when intervalley scattering is accounted for. (e) Magnification of the minibands in (c) near zero energy. Δ_+ and Δ_- are the gaps opened at the two intersection points highlighted by the green dots in (d). (f) Δ_+ and Δ_- as functions of U, for the same superlattice periodicity.

pseudospin $|-x\rangle$, as if the intervalley backscattering is absent. Similarly, the condition for maximum constructive interference for transmission of the pseudospin $|+x\rangle$ state is

$$K + q_h = n\frac{\pi}{W}, \quad K - q_e = m\frac{\pi}{L-W}. \tag{2}$$

The quantitative difference between Eqs. (1) and (2) implies pseudospin-dependent Klein tunneling that is controlled by L, W, and U.

The effect of intervalley backscattering is most significant under the maximum destructive interference in transmission [cf. Fig. 1(b)]. For pseudospin $|-x\rangle$, this occurs under

$$K - q_h = \left(n + \frac{1}{2}\right)\frac{\pi}{W}, \quad K + q_e = \left(m + \frac{1}{2}\right)\frac{\pi}{L-W}. \tag{3}$$

For pseudospin $|+x\rangle$, the condition becomes

$$K + q_h = \left(n + \frac{1}{2}\right)\frac{\pi}{W}, \quad K - q_e = \left(m + \frac{1}{2}\right)\frac{\pi}{L-W}. \tag{4}$$

As the number of periods increases, these conditions of maximum intervalley backscattering will introduce transport gaps. The energy where the transport gaps appear, with respect to the Dirac point, are determined only by the superlattice periodicity L, as we show below through the zone-folding picture [Fig. 1(d)]. In the meantime, Eqs. (1)–(4) imply that the size of the transport gaps is controlled by L, W, and U together.

For a quantitative characterization of the superlattice minibands with the intervalley backscattering effects, we calculate the energy dispersion and pseudospin textures using the standard tight-binding Hamiltonian with nearest-neighbor hopping

$$H = \sum\nolimits_i \varepsilon_i c_i^\dagger c_i - t\sum\nolimits_{\langle i,j\rangle}(c_i^\dagger c_j + H.c.), \tag{5}$$

$c_i^\dagger$ (c_i) is the creation (annihilation) operator at site i, ε_i is the on-site potential that describes the superlattice potential, and the second term is the nearest-neighbor hopping with $t \approx 2.8$ eV.

In the y (armchair) direction, the Hamiltonian has the translational invariance of the pristine graphene lattice, and in the x (zigzag) direction it is also periodic with the superlattice potential $V(x) = V(x + L)$. Thus, the eigenstates can be written in Bloch form, $\varphi_{\vec{k}}(\vec{r}) = u_{\vec{k}}(\vec{r})e^{i\vec{k}\cdot\vec{r}}$, where $u_{\vec{k}}(\vec{r})$ is a periodic function with the above periodicities in x and y directions. $u_{\vec{k}}(\vec{r})$ satisfy $H(\vec{k})u_{\vec{k}}(\vec{r}) = E(\vec{k})u_{\vec{k}}(\vec{r})$, where $H(\vec{k}) \equiv e^{-i\vec{k}\cdot\vec{r}}He^{i\vec{k}\cdot\vec{r}}$. The eigenvalues $E(\vec{k})$ give the superlattice band dispersion. Notably, upon adopting the form of the Kronig-Penney potential [cf. Fig. 1(a)], i.e., with the potential minima being zero and the potential maxima being U, the original Dirac point shifts from zero to $(W/L)U$.

Figures 1(c) shows an example of the superlattice energy bands, with $U = 0.5$ eV, $L = 40a \approx 10$ nm, $W = 20a \approx 5$ nm, in which a is the lattice constant of graphene. The basic features include the anisotropic renormalization of the Dirac cones and generation of new Dirac points due to intravalley scattering, as reported in Refs. [7,32]. As mentioned above, the original Dirac points are at an energy of $E_D^{(0)} = U/2$. The group velocity along x remains at a pristine value of v_0 and is reduced along y. New Dirac points are created at energies of $E_D^{(n)} = E_D^{(0)} \pm \hbar v_0 nG$, $G \equiv \pi/L$. The locations of the new Dirac points can be intuitively found from the schematic zone-folding scheme of the superlattice dispersion at $k_y = 0$, as Fig. 1(d) illustrates.

Besides these new Dirac points, zone folding also leads to intersections of bands of common pseudospin orientation. As highlighted in the zone-folding scheme in Fig. 1(d), the intersection of bands of pseudospin $|-x\rangle$ occurs at energies of $E_-^{(n)}$ alternatively at the boundary and center of the minizone, while bands of pseudospin $|+x\rangle$ intersect at a completely different set of energies of $E_+^{(n)}$. The gapping of these intersection points requires intervalley scattering, since the two branches that run into each other are from the two valleys.

Our calculation accounting for the intervalley scattering finds sizable gaps opened up at these band crossings at $E_\pm^{(n)}$ [indicated by the arrows in Fig. 1(c)]. Figure 1(e) is a magnification of the band dispersion near zero energy with a cut at $k_y = 0$, which includes a pair of Dirac points, a gapped crossing point for pseudospin $|+x\rangle$ in the zone center, and a gapped crossing point for $|-x\rangle$ on the zone boundary. These correspond, respectively, to the new Dirac points at energy $E_D^{(-1)}$ and the crossing points at energies $E_+^{(-1)}$ and $E_-^{(-2)}$, as highlighted by the gray and green circles in the zone-folding scheme in Fig. 1(d). Within the staggered gaps of Δ_+ and Δ_-, the minibands are pseudospin polarized. In particular, all states with $k_y = 0$ are fully polarized in either the $|-x\rangle$ or $|+x\rangle$ pseudospin states. Remarkably, intervalley backscattering makes energy windows for polarized pseudospin transport in the superlattice possible.

Figure 1(f) plots the pseudospin gaps as functions of U, fixing $L = 40a$ and $W = 20a$. Although the superlattice period L is much larger than the lattice constant a, intervalley backscattering by the potential steps introduces sizable gaps of O(10) meV. The magnitudes of the gaps are nonmonotonic with an increase in U, but rather have

oscillations that are out-of-phase between the two pseudospin gaps. Remarkably, the zeros of Δ_- and Δ_+ are given by the scattering resonances in Eqs. (1) and (2), respectively, for the cancellation of intervalley backscattering in individual periods of the superlattice. Likewise, the maximal intervalley backscattering conditions, Eqs. (3) and (4), predict maximal values of the gaps Δ_- and Δ_+, respectively, while the envelope of these maxima is a linear function of U. Equations (1)–(4) serve as simple guidelines to design a superlattice with potential for engineering pseudospin gaps at an arbitrary Fermi energy.

The pseudospin gaps Δ_- and Δ_+, as functions of potential strength U, can also be obtained from the continuum model that leads to transcendental equations. Consider normal incidence, we have the wave function in the barrier region

$$\varphi(x) = Ae^{i\alpha x} + Be^{-i\alpha x},$$

where $\alpha = K - q_h$ for pseudospin $|-x\rangle$ and $\alpha = K + q_h$ for pseudospin $|+x\rangle$. In the well region

$$\varphi(x) = Ce^{i\beta x} + De^{-i\beta x},$$

where $\beta = K \pm q_e$ for pseudospin $|\mp x\rangle$. $q_h = (U - E)/(\hbar v_0)$ and $q_e = E/(\hbar v_0)$ are the Fermi wavevectors in the barrier and well regions, respectively, as measured from the valley center [cf. Fig. 1(b)]. On the other hand, $\varphi(x)$, as a solution of the superlattice Hamiltonian, must have the Bloch form $\varphi(x) = u(x)e^{ik_x x}$, with $u(x)$ having the superlattice periodicity L, so $\varphi(x + L) = \varphi(x)e^{ik_x L}$. This, together with the continuity of the wave function and its derivative, leads to the following transcendental equations that need to be satisfied by the energy eigenvalue E and k_x. For the Bloch state of pseudospin $|-x\rangle$, the equation reads

$$\begin{aligned} &-\frac{(K-q_h)^2+(K+q_e)^2}{2(K-q_h)(K+q_e)}\sin[(K-q_h)W] \\ &\times \sin[(K+q_e)(L-W)] \\ &+ \cos[(K-q_h)W]\cos[(K+q_e)(L-W)] = \cos(k_x L), \end{aligned} \tag{6}$$

Under given parameters U, L, and W, the range of values of E where the above equation cannot be satisfied corresponds to the pseudospin gap Δ_-, in which the Bloch states of $|-x\rangle$ are absent. Similarly, for pseudospin $|+x\rangle$, we have

$$\begin{aligned} &-\frac{(K+q_h)^2+(K-q_e)^2}{2(K+q_h)(K-q_e)}\sin[(K+q_h)W] \\ &\times \sin[(K-q_e)(L-W)] \\ &+ \cos[(K+q_h)W]\cos[(K-q_e)(L-W)] = \cos(k_x L), \end{aligned} \tag{7}$$

which determines the pseudospin gap Δ_+. The different forms of the two transcendental equations underline the facts that Δ_- and Δ_+ occur alternatively in energy [Fig. 1(e)] and that the magnitudes of Δ_- and Δ_+ have different dependences on U [Fig. 1(f)]. Solutions of the transcendental equations are in excellent agreement with the curves shown in Fig. 1(f), where the pseudospin gaps are extracted from the superlattice band structure directly calculated using the tight-binding Hamiltonian.

B. Valley-selective transmission through superlattice barriers

When such a superlattice is used as a tunneling barrier, its staggered pseudospin gaps, combined with the valley-contrasted pseudospin chirality in pristine graphene, lead to valley-selective Klein tunneling. In the original context where Klein tunneling is discussed, intervalley scattering is not considered, and the orthogonality of the pseudospin configurations in the forward and backward propagating states in the same valley is the reason for perfect transmission upon the normal incidence. Upon scattering by a single potential barrier, one generally expects that the perfect Klein tunneling is no longer there in the presence of strong intervalley scattering, which turns on the backscattering channel. The main finding here is that, in a periodically arranged barrier array, the periodicity introduces a condition for the destructive or construction interference of the intervalley backscattering by multiple barriers, which can either restore the perfect transmission (reminiscent of the original Klein tunneling) or completely quench the transmission with the opening of a transport gap. Remarkably, the transport gaps for pseudospins $|-x\rangle$ and $|+x\rangle$ occur alternatively in energy, as evident from the zone-folding picture shown in Fig. 1(d), where the two green dots mark the location of the gaps for $|-x\rangle$ (blue) and $|+x\rangle$ (red) pseudospin branches. This makes the valley-selective Klein tunneling phenomenon possible.

We consider finite periods of a graphene superlattice connected on two sides to semi-infinite pristine graphene leads, as shown in Fig. 2(a). With the pseudospin textures of the Dirac cones in graphene leads, the incident electron has its valley index locked with the sublattice pseudospin, i.e., the K ($-K$) valley electron has pseudospin $|-x\rangle$ ($|+x\rangle$) for normal incidence from the left. Transmission from one of the valleys can then be selectively blocked, due to the absence of the corresponding pseudospin state inside the staggered gaps in the superlattice barrier, as Fig. 2(a) illustrates.

The valley-dependent scattering by the superlattice barrier is calculated with the tight-binding Hamiltonian in Eq. (5), using the recursive Green function technique [33]. Figure 2(b) shows the calculated valley-conserved and valley-flip transmission and reflection coefficients under normal incidence ($k_y = 0$), for a 30-period superlattice barrier with $U = 0.5\,\text{eV}$, $L = 40a$, and $W = 20a$. In the shaded energy window that corresponds to the

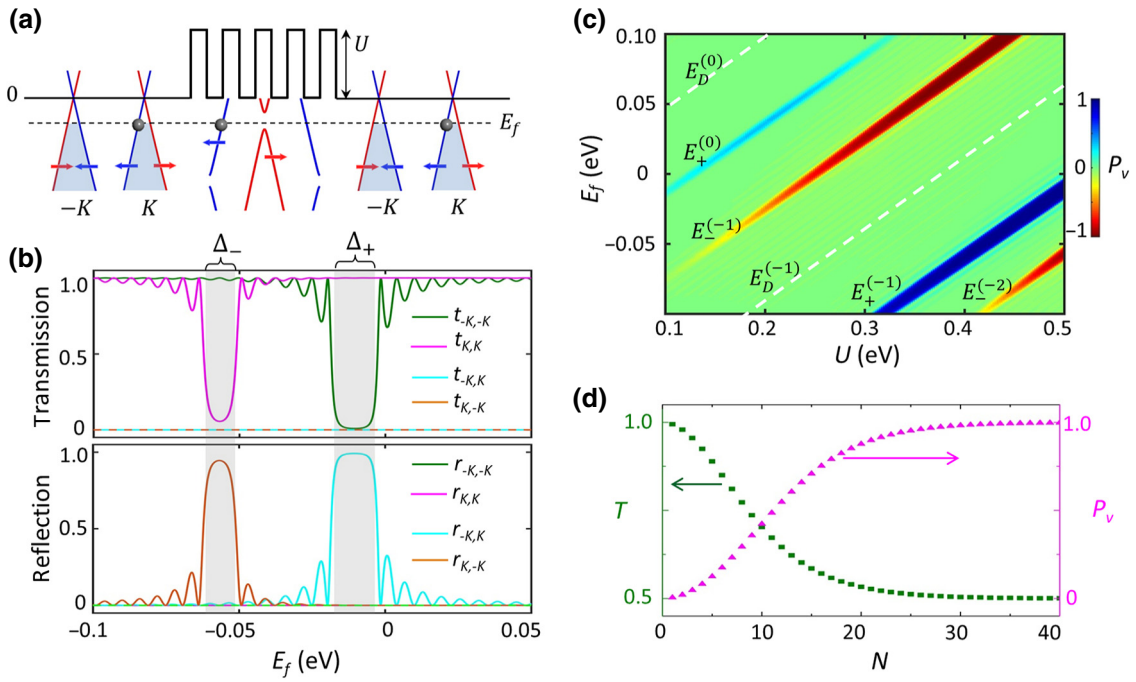

FIG. 2. Valley-selective transmission through superlattice barrier. (a) Schematic of a superlattice barrier connected to graphene leads on two sides. For incidence at energy E_f from the left, transmission in the $-K$ valley is blocked due to the absence of $|+x\rangle$ pseudospin states inside the Δ_+ gap of the superlattice dispersion [cf. Fig. 1(e)]. (b) Valley-resolved transmission (t) and reflection (r) coefficients under normal incidence. Barrier height $U = 0.5\,\text{eV}$. (c) Valley polarization (P_v) of the transmission as a function of U and Fermi energy E_f under an unpolarized normal incidence. (d) Valley polarization and transmission probability T as functions of superlattice period N. All calculations here use superlattice configuration $L = 40a \approx 10\,\text{nm}$, $W = 20a \approx 5\,\text{nm}$ [cf. Fig. 1(a)]. $N = 30$ in (b) and (c).

pseudospin gap Δ_+ shown in Fig. 1(e), we find perfect valley-conserving transmission for incidence in valley K and perfect valley-flip reflection for incidence in valley $-K$. The energy window Δ_- exhibits the same behavior with opposite valley polarity for the allowed and blocked transmission. In the neighborhood of Δ_+ and Δ_-, multiple intervalley scatterings by the step-shaped edges in the potential also give rise to closely spaced scattering resonances, which will develop into minibands in the infinite period superlattice. The overall transmission probability, $T \equiv (t_{K,K} + t_{-K,-K} + t_{K,-K} + t_{-K,K})/2$, equals 50%, exhibiting the full valley selectivity within the pseudospin gaps, and approaches one far outside where perfect Klein tunneling is restored in both valleys.

Figure 2(c) plots $P_v \equiv (1/2T)(t_{K,K} + t_{-K,K} - t_{-K,-K} - t_{K,-K})$, the valley polarization of the normal incidence transmission, as a function of the incident energy E_f and barrier height U, for the same barrier geometry as that in Fig. 2(b). In the plotted range, we find four energy windows of valley-selective Klein tunneling, corresponding, respectively, to the pseudospin gaps Δ_+ at $E_+^{(0)}$ and $E_+^{(-1)}$ and Δ_- at $E_-^{(-1)}$ and $E_-^{(-2)}$, as illustrated in the zone-folding scheme in Fig. 1(d). The transmission has nearly perfect valley polarization in these pseudospin gaps with alternating valley polarity. Outside the gaps, the valley polarization sharply drops to zero. This makes sharp control of the valley-filtering functionality of the junction possible by electrostatic control.

C. Angle-integrated valley polarization

The valley filter here functions in the coherent Klein tunneling regime, requiring the entire width of the superlattice to be small relative to the electron mean free path, which can reach over 10 μm in high-quality graphene [3,4]. This allows the use of a few tens of periods, with $L \sim \text{O}(10)$ nm limited by the lithography of electrodes, which are sufficient to achieve a high-efficiency valley filter, as Fig. 2(d) shows. The filtered valley current, on other hand, can be harvested into channels beyond the ballistic limit, as long as the valley polarity does not cancel out after integration over the incidence-outgoing angle. The angle-averaged valley polarity is therefore a key figure of merit for practical applications.

Figure 3(b) shows the valley polarization P_v and transmission probability T as functions of the incident-outgoing angle $\phi = \tan^{-1}(k_y/k_x)$, for a 20-period superlattice barrier with $U = 0.5\,\text{eV}$, $L = 40a$, and $W = 20a$. Remarkably, a large valley polarization is achieved with the same sign over a significant range of angles. At angle $|\phi| > 60°$,

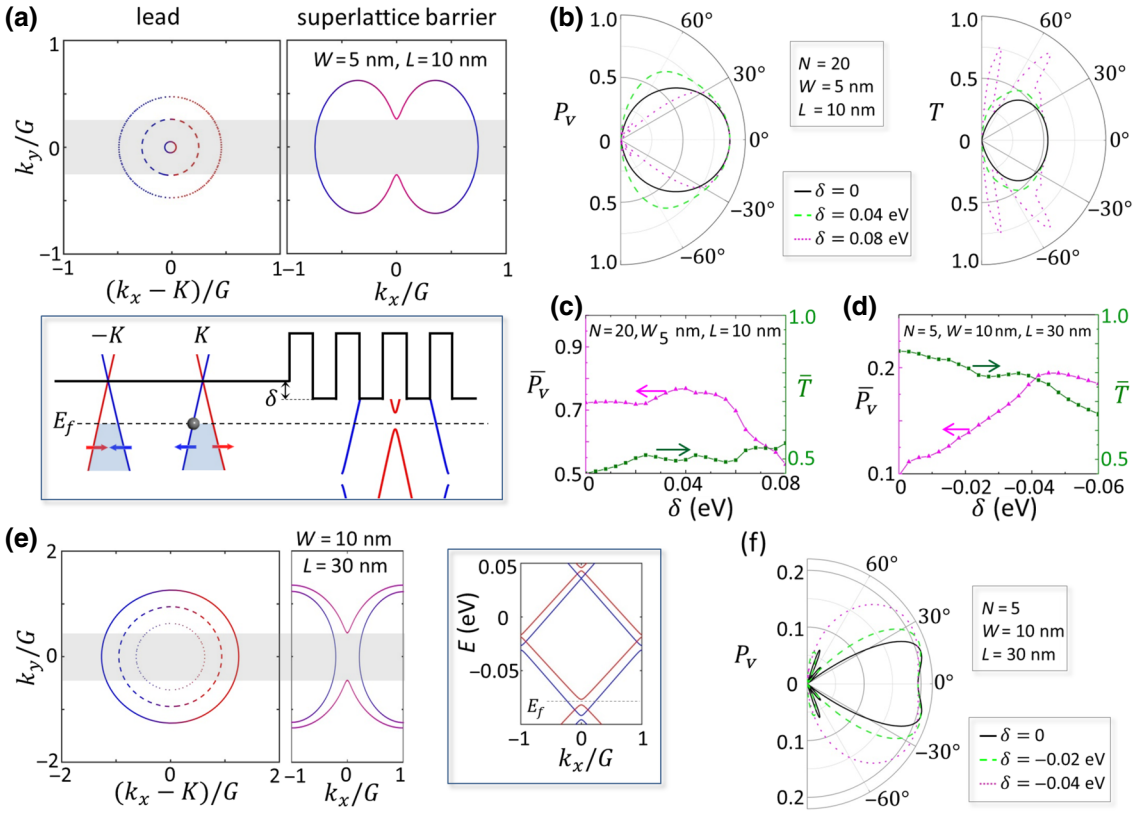

FIG. 3. Valley-filtering performance under angle integration. (a) Energy contour inside the Δ_+ gap of the superlattice dispersion, in comparison with the lead Fermi surface, which can be independently gate controlled. Solid, dashed, and dotted lead Fermi surfaces correspond to parameters $\delta = 0$, 0.04, and 0.08 eV, respectively (cf. inset). Pseudospin projections with $|+x\rangle$ and $|-x\rangle$ are color coded in red and blue, respectively. (b) Valley polarization (P_v) and probability (T) of transmission as functions of incidence angle, at $\delta = 0$, 0.04, and 0.08 eV. (c) Angle-averaged valley polarization $\overline{P_v}$ and transmission probability $\bar{T}$, as functions of δ. (b) and (c) use a 20-period superlattice barrier with $L = 40a \approx 10\,\text{nm}$, $W = 20a \approx 5\,\text{nm}$. (d)–(f) Similar plots for a superlattice of wider barriers and spacing: $L = 120a \approx 30\,\text{nm}$ and $W = 40a \approx 10\,\text{nm}$, where energy dispersion at $k_y = 0$ is shown in the inset. (d) and (f) show the performance using only five periods of such a superlattice barrier.

where P_v drops to zero, the transmission probability T is already negligible. This leads to a pronounced angle-averaged valley polarization ($\overline{P_v}$) exceeding 70%, with an angle-averaged transmission probability of $\bar{T} \sim 50\%$.

The wide-angle valley filtering and large $\overline{P_v}$ arise from the fact that the pseudospin gap exists over a range of k_y that is comparable to or larger than that of the lead Fermi surface. For the superlattice barrier used in the calculation of Fig. 3(b), we show its energy contour inside the gap Δ_+, color coded with the pseudospin texture, in Fig. 3(a). The shaded area denotes the k_y range over which pseudospin state $|+x\rangle$ is absent. As long as the Fermi surface in the graphene lead does not exceed this range, the conservation of k_y and pseudospin in scattering leads to valley filtering over the entire angle range where transmission is significant. This is tested for several sizes of the Fermi surface in the graphene lead, which is tuned through an electrostatic shift, δ, of the lead Dirac points [cf. Fig. 3(a), inset]. As shown in Figs. 3(b) and 3(c), the angle-averaged valley polarization remains large until the lead Fermi surface gets significantly larger than the shaded k_y range in Fig. 3(a), where both pseudospin states become available at a large oblique angle. For the given superlattice, a large angle-integrated valley-filtering effect is expected for $\delta \lesssim 0.04\,\text{eV}$ [Fig. 3(c)].

Figures 3(d)–3(f) show a further example of a superlattice barrier, where a larger period of $L = 120a \approx 30\,\text{nm}$ leads to a narrower k_y range of pseudospin-polarized spectrum. Large $\overline{P_v}$ is obtained for $\delta \lesssim -0.04\,\text{eV}$ and, remarkably, by using only a five-period barrier, the angle-averaged valley polarization can already reach about 20% [cf. Fig. 3(d)].

III. DISCUSSION

For an electrostatically defined superlattice, the potential steps cannot be made atomically sharp. The lateral length scale of the potential step is determined by the vertical distance between the local gate and graphene, which can be made as small as about a nanometer using

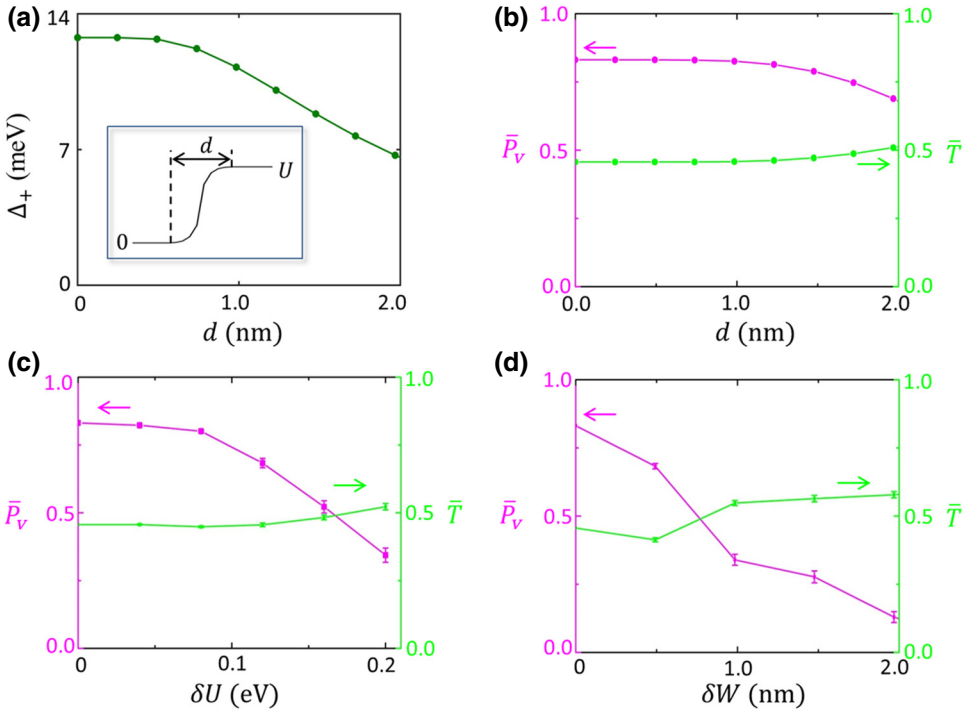

FIG. 4. Valley-filtering performance under imperfections. (a) Pseudospin gap Δ_+ as a function of d, which quantifies smoothening of the potential steps, as shown in the inset. (b) Angle-averaged valley polarization ($\overline{P_v}$) and probability ($\bar{T}$) of transmission, as functions of d. (c) $\overline{P_v}$ and $\bar{T}$ in the presence of statistical fluctuation in barrier heights. (d) $\overline{P_v}$ and $\bar{T}$ in the presence of statistical fluctuation in barrier widths. $L = 40a \approx 10\,\text{nm}$, $W = 20a \approx 5\,\text{nm}$, and 30 periods of such a superlattice barrier are used in (b)–(d).

hexagonal boron nitride (h-BN) as the gate dielectric [34]. In general, a superlattice with smoother potential steps will have a smaller Fourier component responsible for intervalley scattering. A reduction of the pseudospin gap size is therefore expected. To quantify such an effect on valley filtering, we calculate transmission through a superlattice barrier with a potential step described by a hyperbolic function, i.e., $U/2\{[(\tanh 6x/d)/\tanh 3] + 1\}$ in $x \in [(-d/2), (d/2)]$, with d characterizing the length scale [cf. Fig. 4(a), inset].

Figure 4(a) plots the pseudospin gap Δ_+ as a function of d, for a superlattice with $L = 40a$, $W = 20a$, and $U = 0.5\,\text{eV}$. The gap size drops by half at $d = 8a \approx 2\,\text{nm}$. While this results in a narrower window for valley-selective tunneling, the effect on the performance inside the gap is less significant. Figure 4(b) plots the valley-filtering effect through 30 periods of the smoothened barriers. The angle-averaged valley polarization $\overline{P_v}$ shows a remarkable robustness to the smoothening of potential steps, still reaching about 70% at $d = 8a$.

We also examine the effect of statistical fluctuations in gate potential and gate width. The fluctuation of the gate potential is simulated by changing the height of barrier i from U to $U + \delta U_i$, where δU_i is randomly chosen from a uniform distribution in a range $[(-\delta U/2), (\delta U/2)]$, with δU characterizing the fluctuation strength. Similarly, fluctuation of the gate width is accounted for by adding a random amount to the width of each barrier, with a fluctuation strength of δW. We find that the valley-filter performance is remarkably robust against fluctuations in the gate-potential strength. Valley polarization $\overline{P_v}$ has a negligible drop for δU up to 20% of the barrier height U [cf. Fig. 4(c)]. On the other hand, $\overline{P_v}$ is more sensitive to fluctuation of the gate width [Fig. 4(d)], which requires the lithography error to be controlled on about a nanometer scale.

We also note that, when the superlattice period L is an integer number of $3a$, the pseudospin gaps Δ_+ and Δ_- are both located in the vicinity of the new Dirac points ($E_D^{(n)}$), as shown in the inset of Fig. 3(e). The small offset between Δ_+ and Δ_- comes from the trigonal warping of the graphene Dirac cone. In such a case, with Δ_+ and Δ_- close in energy, an electrostatic switch of valley-filtering polarity at a fixed Fermi energy can be realized with a smaller change of barrier height.

While the calculations shown here are for barriers parallel to the armchair direction, we also obtain similar results using barriers along other chiral directions, except that the pseudospin gaps are smaller. The effect disappears only when the potential barriers are fully parallel to the zigzag direction, where the intervalley scattering then vanishes in the transport direction. For gate-defined barriers, while it is favorable and practical to fabricate the gates parallel to the armchair direction, high-precision control of the fabrication angle is not necessary.

ACKNOWLEDGMENTS

X.A. acknowledges support by the Hebei Funds for Distinguished Young Scientists (Grant No. A201808076) and the Hebei Hundred Excellent Innovative Talents (Grant No. SLRC2017035). W.Y. acknowledges support by the

Seed Funding for Strategic Interdisciplinary Research Scheme of HKU and Collaborative Research Funds (Grant No. C7036-17W) of RGC.

[1] O. Klein, Die reflexion von elektronen an einem potentialsprung nach der relativistischen dynamik von dirac, Z. Phys. **53**, 157 (1929).

[2] M. Katsnelson, K. Novoselov, and A. Geim, Chiral tunnelling and the Klein paradox in graphene, Nat. Phys. **2**, 620 (2006).

[3] L. Wang, I. Meric, P. Huang, Q. Gao, Y. Gao, H. Tran, T. Taniguchi, K. Watanabe, L. Campos, and D. Muller, One-dimensional electrical contact to a two-dimensional material, Science **342**, 614 (2013).

[4] L. Banszerus, M. Schmitz, S. Engels, M. Goldsche, K. Watanabe, T. Taniguchi, B. Beschoten, and C. Stampfer, Ballistic transport exceeding 28 μm in CVD grown graphene, Nano Lett. **16**, 1387 (2016).

[5] A. F. Young and P. Kim, Quantum interference and Klein tunnelling in graphene heterojunctions, Nat. Phys. **5**, 222 (2009).

[6] V. V. Cheianov, V. Fal'ko, and B. Altshuler, The focusing of electron flow and a Veselago lens in graphene pn junctions, Science **315**, 1252 (2007).

[7] C.-H. Park, L. Yang, Y.-W. Son, M. L. Cohen, and S. G. Louie, Anisotropic behaviours of massless Dirac fermions in graphene under periodic potentials, Nat. Phys. **4**, 213 (2008).

[8] C.-H. Park, Y.-W. Son, L. Yang, M. L. Cohen, and S. G. Louie, Electron beam supercollimation in graphene superlattices, Nano Lett. **8**, 2920 (2008).

[9] J. Garcia-Pomar, A. Cortijo, and M. Nieto-Vesperinas, Fully Valley-Polarized Electron Beams in Graphene, Phys. Rev. Lett. **100**, 236801 (2008).

[10] Q. Wilmart, S. Berrada, D. Torrin, V. H. Nguyen, G. Fève, J.-M. Berroir, P. Dollfus, and B. Plaçais, A klein-tunneling transistor with ballistic graphene, 2D Mater. **1**, 011006 (2014).

[11] S. Chen, Z. Han, M. M. Elahi, K. M. Habib, L. Wang, B. Wen, Y. Gao, T. Taniguchi, K. Watanabe, and J. Hone, Electron optics with pn junctions in ballistic graphene, Science **353**, 1522 (2016).

[12] L. Brey and H. A. Fertig, Emerging Zero Modes for Graphene in a Periodic Potential, Phys. Rev. Lett. **103**, 046809 (2009).

[13] O. Gunawan, B. Habib, E. De Poortere, and M. Shayegan, Quantized conductance in an AlAs two-dimensional electron system quantum point contact, Phys. Rev. B **74**, 155436 (2006).

[14] A. Rycerz, J. Tworzydlo, and C. W. J. Beenakker, Valley filter and valley valve in graphene, Nat. Phys. **3**, 172 (2007).

[15] D. Xiao, W. Yao, and Q. Niu, Valley-contrasting Physics in Graphene: Magnetic Moment and Topological Transport, Phys. Rev. Lett. **99**, 236809 (2007).

[16] W. Yao, D. Xiao, and Q. Niu, Valley-dependent optoelectronics from inversion symmetry breaking, Phys. Rev. B **77**, 235406 (2008).

[17] R. V. Gorbachev, J. C. W. Song, G. L. Yu, A. V. Kretinin, F. Withers, Y. Cao, A. Mishchenko, I. V. Grigorieva, K. S. Novoselov, L. S. Levitov, and A. K. Geim, Detecting topological currents in graphene superlattices, Science **346**, 448 (2014).

[18] M. Sui, G. Chen, L. Ma, W.-Y. Shan, D. Tian, K. Watanabe, T. Taniguchi, X. Jin, W. Yao, D. Xiao, and Y. Zhang, Gate-tunable topological valley transport in bilayer graphene, Nat. Phys. **11**, 1027 (2015).

[19] Y. Shimazaki, M. Yamamoto, I. V. Borzenets, K. Watanabe, T. Taniguchi, and S. Tarucha, Generation and detection of pure valley current by electrically induced Berry curvature in bilayer graphene, Nat. Phys. **11**, 1032 (2015).

[20] D. Gunlycke and C. T. White, Graphene Valley Filter Using a Line Defect, Phys. Rev. Lett. **106**, 136806 (2011).

[21] I. Martin, Y. M. Blanter, and A. F. Morpurgo, Topological Confinement in Bilayer Graphene, Phys. Rev. Lett. **100**, 036804 (2008).

[22] W. Yao, S. A. Yang, and Q. Niu, Edge States in Graphene: From Gapped Flat-Band to Gapless Chiral Modes, Phys. Rev. Lett. **102**, 096801 (2009).

[23] F. Zhang, A. H. MacDonald, and E. J. Mele, Valley Chern numbers and boundary modes in gapped bilayer graphene, PNAS **110**, 10546 (2013).

[24] L. Ju, Z. Shi, N. Nair, Y. Lv, C. Jin, V. J. Jr, C. Ojeda-Aristizabal, H. A. Bechtel, M. C. Martin, A. Zettl, J. Analytis, and F. Wang, Topological valley transport at bilayer graphene domain walls, Nature **520**, 650 (2015).

[25] J. Li, R.-X. Zhang, Z. Yin, J. Zhang, K. Watanabe, T. Taniguchi, C. Liu, and J. Zhu, A valley valve and electron beam splitter, Science **362**, 1149 (2018).

[26] T. Low and F. Guinea, Strain-Induced pseudomagnetic field for novel graphene electronics, Nano Lett. **10**, 3551 (2010).

[27] Z. Wu, F. Zhai, F. M. Peeters, H. Q. Xu, and K. Chang, Valley-Dependent Brewster Angles and Goos-Hanchen Effect in Strained Graphene, Phys. Rev. Lett. **106**, 176802 (2011).

[28] H. Yu, Y. Wu, G.-B. Liu, X. Xu, and W. Yao, Nonlinear Valley and Spin Currents From Fermi Pocket Anisotropy in 2D Crystals, Phys. Rev. Lett. **113**, 156603 (2014).

[29] C. Park, Generation of valley-polarized electron beam in bilayer graphene, J. Appl. Phys. **118**, 244301 (2015).

[30] M. W.-Y. Tu and W. Yao, Switchable valley functionalities of an n−n$^-$−n junction in 2D crystals, 2D Mater. **4**, 025109 (2017).

[31] X.-T. An, J. Xiao, M. W. Y. Tu, H. Yu, V. I. Fal'ko, and W. Yao, Realization of Valley and Spin Pumps by Scattering at Nonmagnetic Disorders, Phys. Rev. Lett. **118**, 096602 (2017).

[32] C.-H. Park, L. Yang, Y.-W. Son, M. L. Cohen, and S. G. Louie, New Generation of Massless Dirac Fermions in Graphene Under External Periodic Potentials, Phys. Rev. Lett. **101**, 126804 (2008).

[33] T. Ando, Quantum point contacts in magnetic fields, Phys. Rev. B **44**, 8017 (1991).

[34] L. Britnell, R. V. Gorbachev, R. Jalil, B. D. Belle, F. Schedin, M. I. Katsnelson, L. Eaves, S. V. Morozov, A. S. Mayorov, and N. M. Peres, Electron tunneling through ultrathin boron nitride crystalline barriers, Nano Lett. **12**, 1707 (2012).